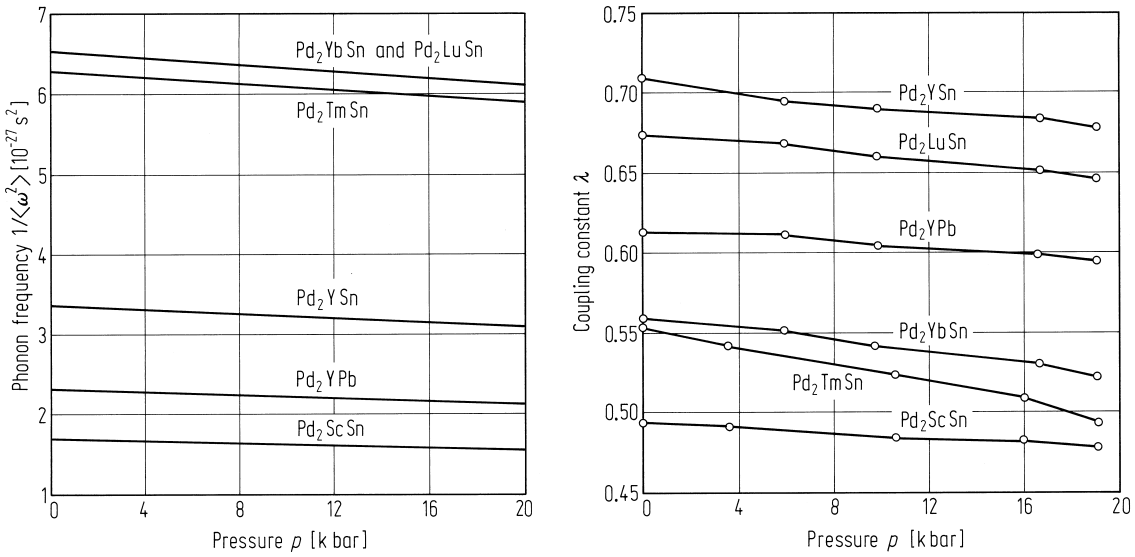

Fig. 333. Pressure dependence of the electron - phonon coupling constant λ and the inverse phonon frequency calculated in the strong coupling limit [84J1].

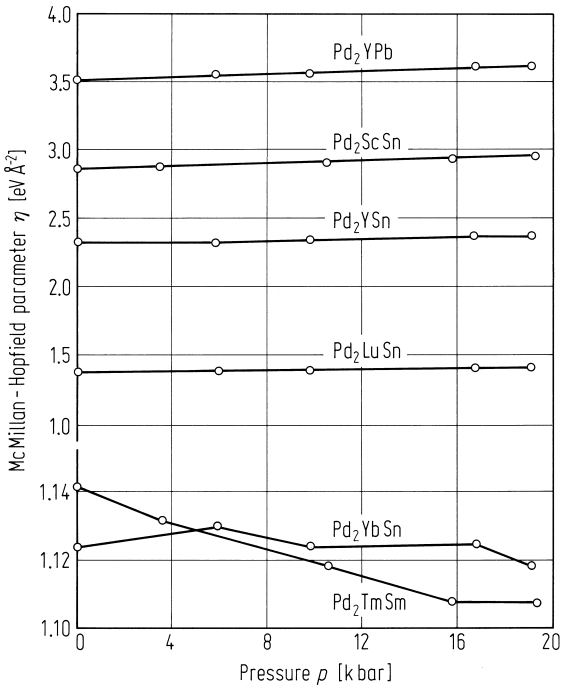

Fig. 335. Calculated pressure dependence of the McMillan-Hopfield parameter η. The insensitivity of η with respect to pressure indicates that the variation of T_c with pressure is due primarily to lattice stiffening [84J1].

1.5.5.7 Thermal properties

This section deals with the specific heat of Heuslers which do not become superconducting. Particular interest has been focused on compounds containing rare earth elements where the effects of the crystal field are important. Attention has also been concentrated on the possibility of discovering new Heavy Fermion systems. The data are analysed assuming electronic, phonon and nuclear contributions.

$$\frac{C}{T} = \gamma + \beta T^2 + \frac{A}{T^2} \tag{67}$$

X_2MnZ X = 3d, 4d

X = 8A: Co, Ni, Pd; 1B: Cu
Z = 3B: In; 4B: Sn; 5B: Sb

Table 70. A, γ, β coefficients as defined in Fig. 336, Debye (Θ_D) and Einstein (Θ_E) temperatures and a weight factor (p) obtained by altering the lattice term to $(1 - p)\ \beta T^3$ and adding a term $pC_E(T)$. T_c and T_N are the ordering temperatures of X_2MnSn, X_2MnIn and X_2MnSb compounds [91F1].

Compound	A [mJ K mol^{-1}]	γ [mJ mol^{-1} K^{-2}]	$\beta(\Theta_D)$ [mJ mol^{-1} K^{-4}]	Θ_E [K]	p	T_c [K]
Co_2MnSn	10.8	17.1	0.152(370)			829
Ni_2MnSn	6.6	13.7	0.353(280)	54	0.012	355
Cu_2MnSn	7.7	4.6	0.698(223)	53	0.026	530
Pd_2MnSn	8.6	12.2	0.690(224)	60	0.026	189
Ni_2MnIn		18.6	0.480(253)	22	0.001	350
Pd_2MnIn		16.2	1.084(193)	20	0.002	(142)
Ni_2MnSb	13.9	12.6	0.811(212)	47	0.003	360

Table 71. Experimental values of the nuclear Schottky coefficient A and the magnetic effective fields on the Mn nuclei, H_{eff}, [91F1].

Compound	A [mJ K mol^{-1}]		H_{eff} [kOe]		
	exp	calc	[91F1]	[70S1]	[70K1]
Co_2MnSn	10.8	12.72			
Ni_2MnSn	6.6	6.12	330 ± 10	313	
Pd_2MnSn	8.6	7.68	374 ± 35		350
Cu_2MnSn	7.7	5.40			
Ni_2MnSb	13.9	9.0			

Table 72. Electronic specific heat coefficients γ [91F1]. Different values for γ_{calc} refer to different sources.

Compound	γ_{exp} [mJ mol^{-1} K^{-2}]	γ_{calc} [mJ mol^{-1} K^{-2}]	$\gamma_{exp}/\gamma_{theor}$
Co_2MnSn	17.7	2.60, 3.48	6.8, 5.08
Ni_2MnSn	13.7	6.80, 7.20, 5.00	2.01, 1.90, 2.74
Cu_2MnSn	4.6	4.00	1.15
Pd_2MnSn	12.2	4.20, 6.00	2.90, 2.03
Ni_2MnIn	18.6	5.72	3.25
Pd_2MnIn	16.2	4.96	3.27
Ni_2MnSb	12.6	5.20	2.42

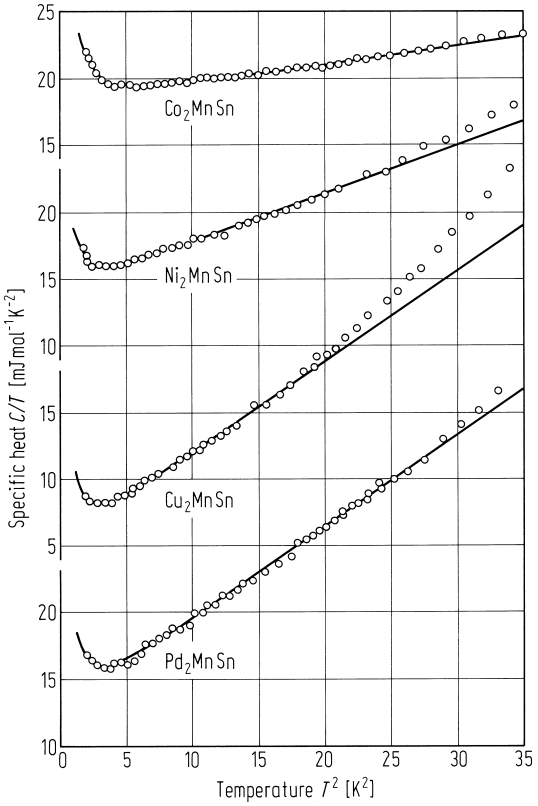

Fig. 336. C/T vs. T^2 for X_2MnSn compounds with X = Co, Ni, Cu, Pd. Circles are experimental points and the solid line is a least squares fit of $C(T) = AT^{-2} + \gamma T + \beta T^3$ to the data (i.e. nuclear Schottky, electronic and nuclear contributions) [91F1].

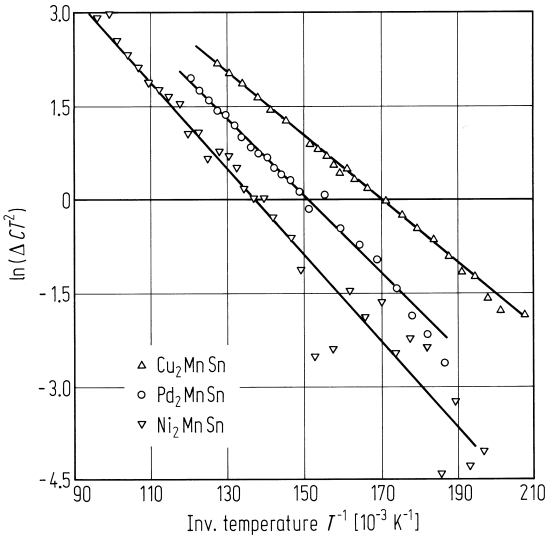

Fig. 337. Einstein contribution to the specific heat $\Delta C(T) = (K/T)^2\exp(-\theta_E/T)$ where K is a constant, for Cu_2MnSn, Pd_2 MnSn, and Ni_2NnSn [91F1].

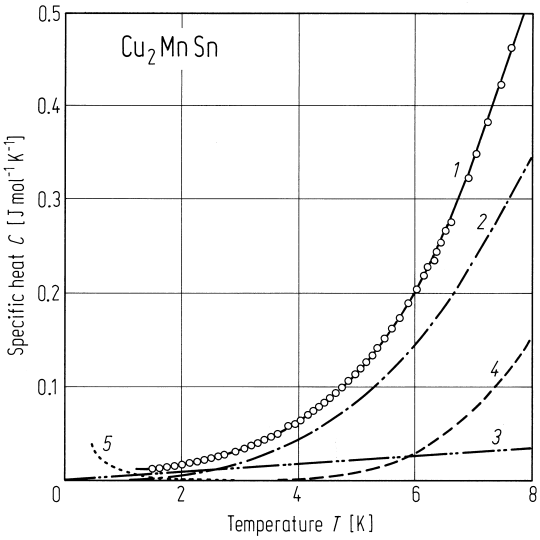

Fig. 338. Cu_2MnSn specific heat data plotted as a function of temperature (circles) experimental data, curve *1* is the fit using the four terms described in Figs. 336 and 337, *2*: lattice term, *3*: electronic term, *4*: Einstein term, *5*: Schottky term [91F1].

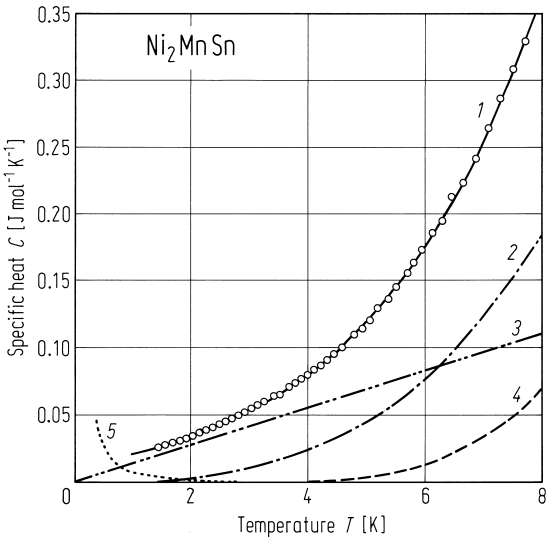

Fig. 339. Ni_2MnSn specific heat C vs. T data. Circles: experimental values; curve *1*: fit; *2*: lattice term, *3*: electronic term; *4*: Einstein term, *5*: Schottky term [91F1].

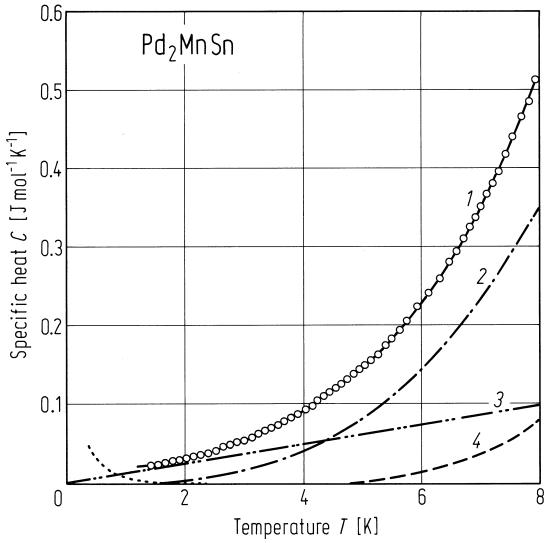

Fig. 340. Specific heat of Pd_2MnSn plotted as a function of temperature. The solid line (curve *1*) represents a four-parameter fit described above, *2*: lattice term, *3*: electronic term, *4*: Einstein term, *5*: Schottky term [91F1].

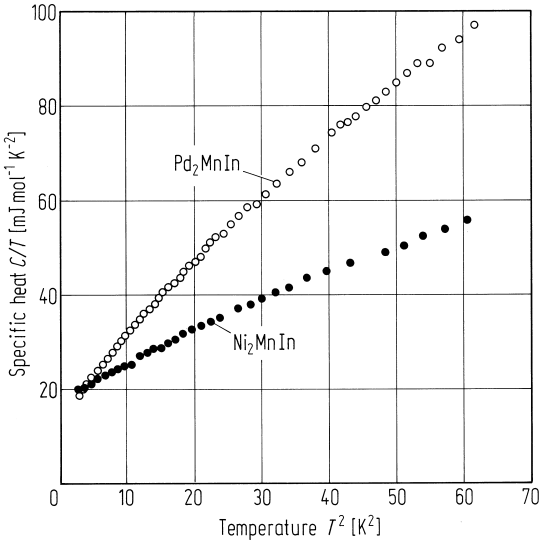

Fig. 341. C/T vs. T^2 data of Pd_2 MnIn and Ni_2 MnIn [91F1].

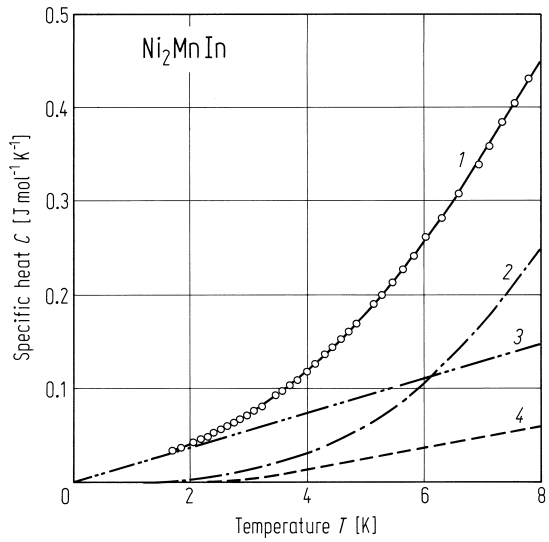

Fig. 342. Specific heat as a function of temperature for Ni_2MnIn. Circles: experimental values, curve *1*: a four parameter fit described above, *2*: lattice term, *3*: electronic term, *4*: Einstein term [91F1].

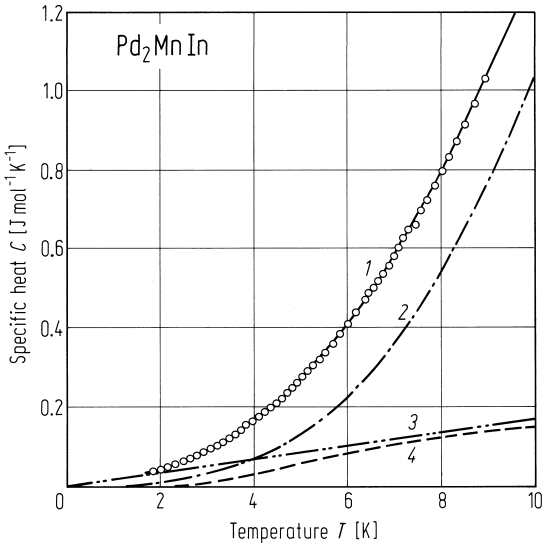

Fig. 343. Pd_2MnIn specific heat plotted as a function of temperature. Circles: experimental data, curve *1*: a four parameter fit, *2*: lattice term, *3*: electronic term, *4*: Einstein term [91F1].

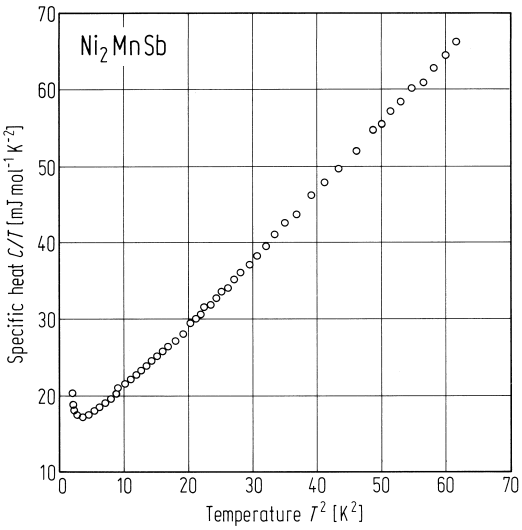

Fig. 344. Specific heat of Ni_2MnSb plotted as C/T vs. T^2 data [91F1].

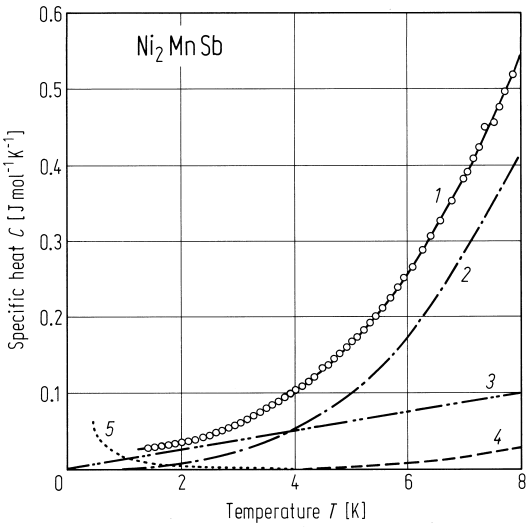

Fig. 345. Ni_2MnSb specific heat C vs. temperature. Circles: experimental values; curve *1*: a four parameter fit; *2*: lattice term, *3*: electronic term, *4*: Einstein term, *5*: Schottky term [91F1].

X = 1B: Cu
Y = 4A: La, Ce, Pr, Nd, Sm, Y, Lu
Z = 3B: In

The properties of the La compound are normal with $\gamma = 2.04$ mJ/(mol·K^2) and a Debye temperature of $\Theta_D = 183$ K. These results have been used in the analysis of the other compounds to estimate the electronic and phonon contributions. Below ≈ 4 K the specific heat of the Ce compound is nearly constant, with the value of γ increasing rapidly [92S1]. The entropy S_{mag} reaches R ln(2) at about 20 K. It has been assumed that the ground state is a doublet which changes to a singlet by a dense Kondo effect below 20 K. Cu_2PrIn exhibits a Schottky-type anomaly around 5 K and it is concluded that the compound is non-magnetic with a singlet ground state. However, both Cu_2NdIn and Cu_2SmIn have sharp transitions at 2 and 3.7 K respectively, indicating long range magnetic order [92S1].

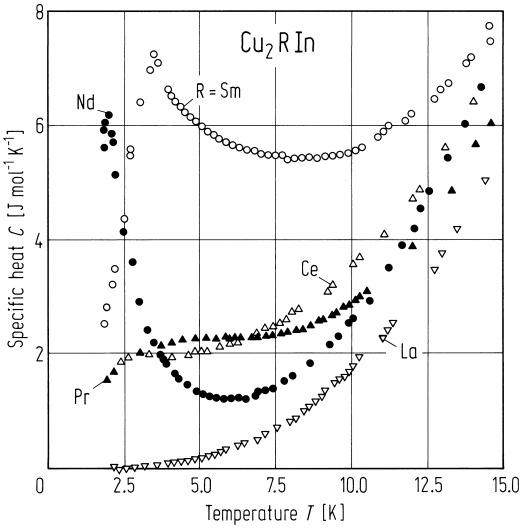

Fig. 346. Temperature dependence of the specific heat for rare earth Heusler compounds Cu_2RIn, R = La, Ce, Pr, Nd, Sm [92S1].

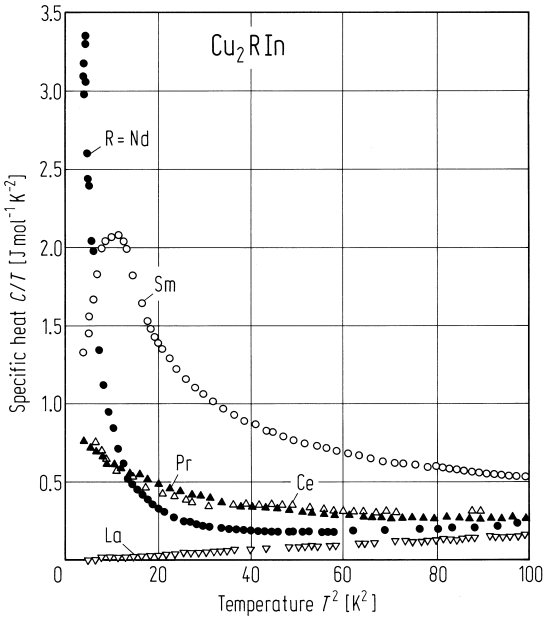

Fig. 347. Curves of specific heat coefficient C/T vs. T^2 for rare earth Heusler compounds Cu_2RIn [92S1].

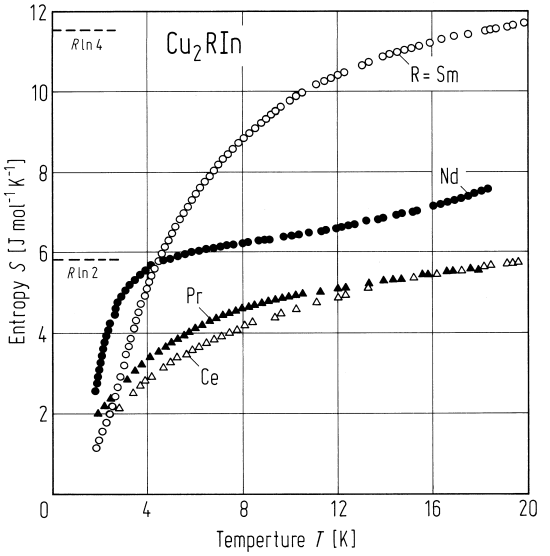

Fig. 348. Temperature dependence of the entropy for rare earth Heusler compounds Cu_2RIn [92S1].

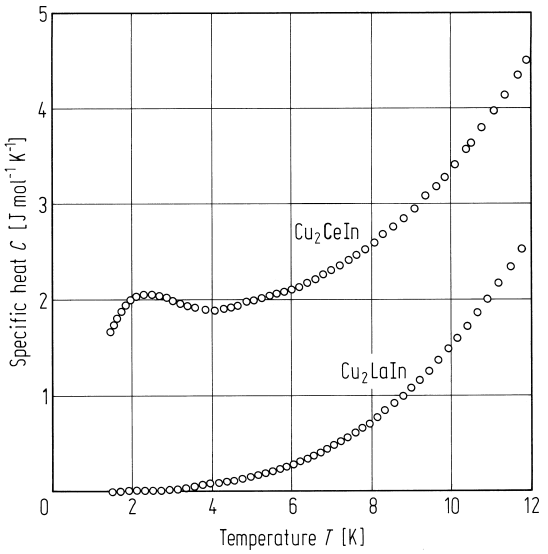

Fig. 349. Specific heat of polycrystalline Cu_2CeIn and Cu_2LaIn [93D1].

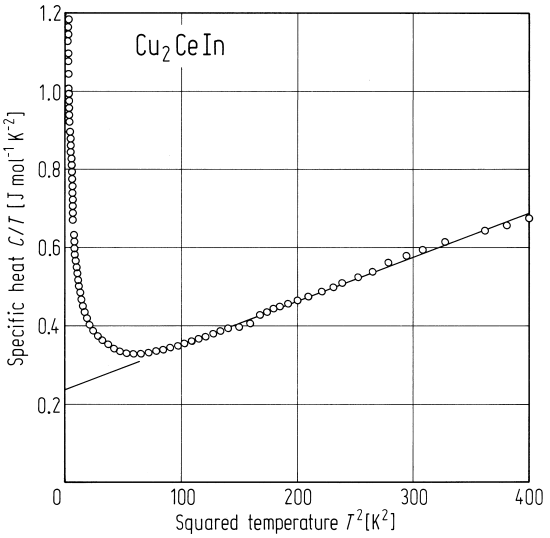

Fig. 350. Temperature dependence of the specific heat C in the form of a C/T vs. T^2 plot for Cu_2CeIn. The solid line represents the relation $C/T = \gamma + \beta T^2$ with γ = 247 mJ/mol·K^2 and β = 1.12 mJ/mol·K^4 [88T1].

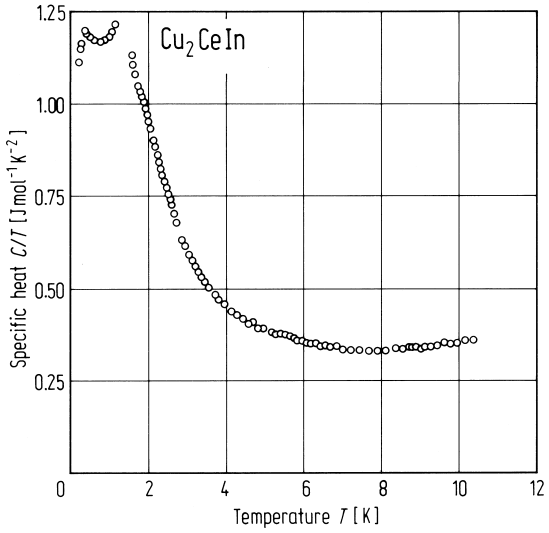

Fig. 351. Temperature dependence of the specific heat C in the form of a C/T vs. T plot below 10 K for Cu_2CeIn [88T1].

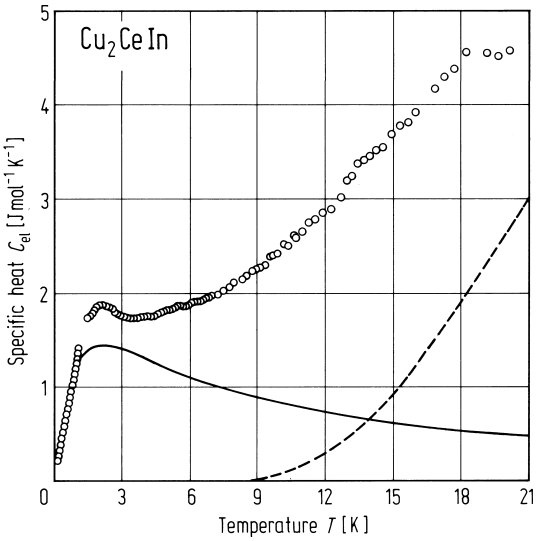

Fig. 352. Temperature dependence of the electronic part of the specific heat, C_{el}, which is evaluated as $C_{el} = C - \beta T^3$ with β given by eq. (67), for Cu_2CeIn. The solid curve represents the result of the Bethe-Ansatz calculation for an S = 1/2 single-impurity Kondo model with T_K = 3.2 K. Also shown by the dashed line is the Schottky contribution to C_{el} with the Γ_7 doublet ground state and the crystalline-electric-field splitting Δ = 98 K [88T1].

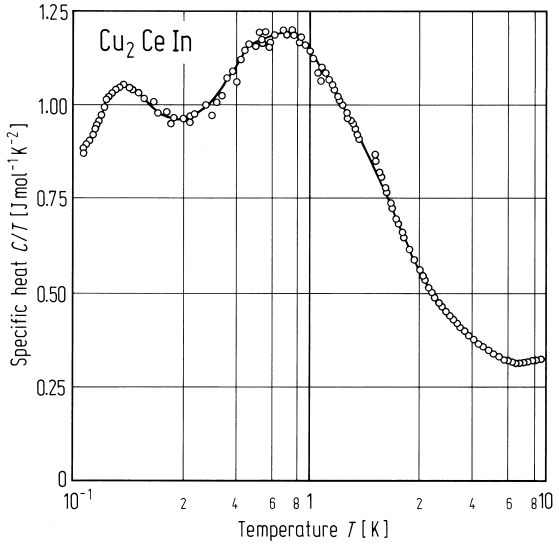

Fig. 353. Temperature dependence of the specific heat coefficient C/T for a Cu_2CeIn single crystal [87O2].

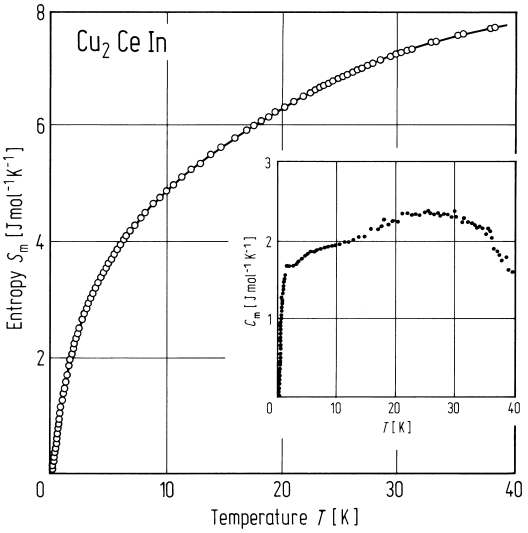

Fig. 354. Temperature dependence of the magnetic entropy for a Cu_2CeIn single crystal. The inset shows the temperature dependence of the magnetic specific heat [87O2].

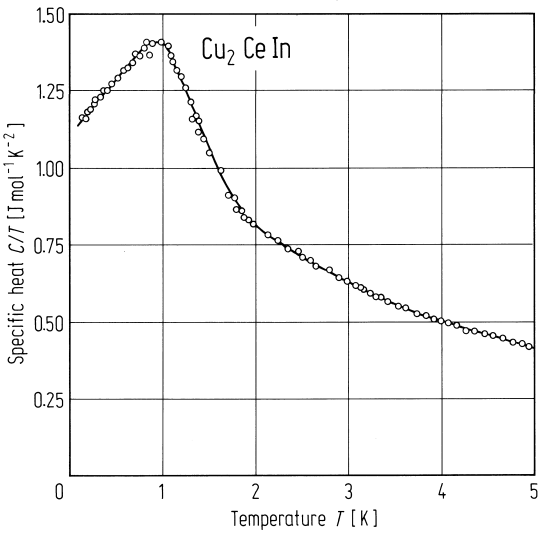

Fig. 355. Specific heat coefficient C/T for Cu_2CeIn [88T3].

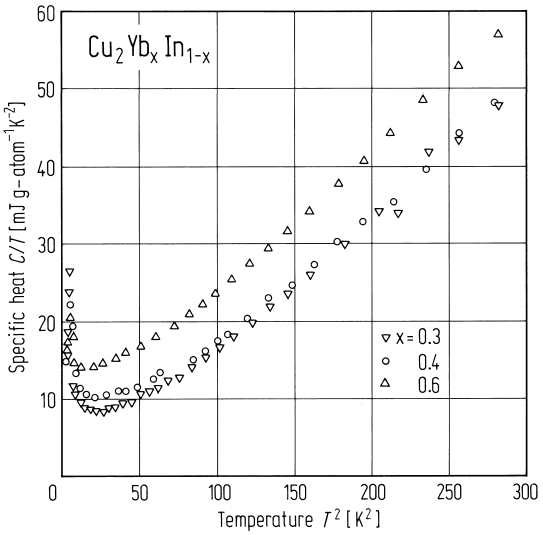

Fig. 356. Specific heat C divided by temperature T vs. T^2 for $Cu_2Yb_xIn_{1-x}$ with x = 0.3, 0.4, 0.6 [87S1].

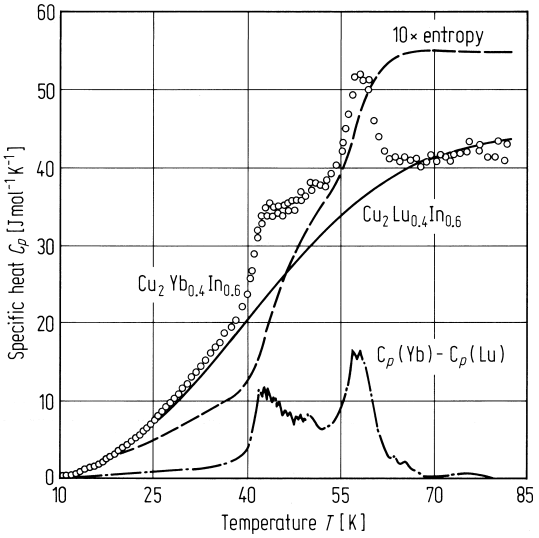

Fig. 357. Temperature dependence of the specific heat of $Cu_2Yb_{0.4}In_{0.6}$, $Cu_2Lu_{0.4}In_{0.6}$, the difference between the two as well as the entropy corresponding to this difference. For a system with 100 % Yb the Yb specific heat and entropy will be 2.5 times larger [87F1].

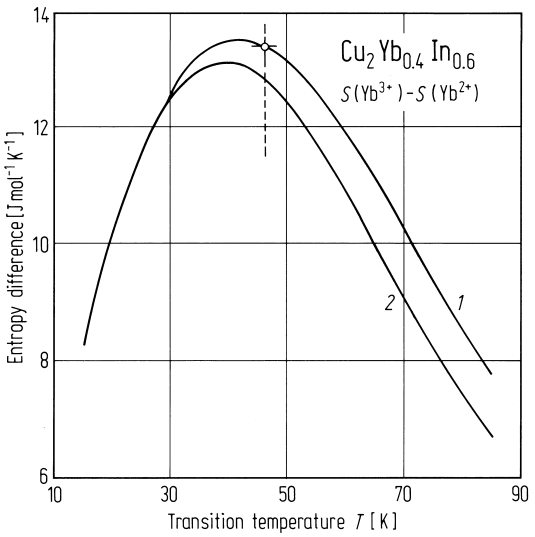

Fig. 358. Theoretically calculated entropy difference between Yb^{3+} and Yb^{2+} in $Cu2Yb_{0.4}In_{0.6}$. Curve *1*: E_0 = 220 K; curve 2: E_0 = 200 K. $A_4 \langle r^4 \rangle$ = 40 K, α = 2.1 [87F1].

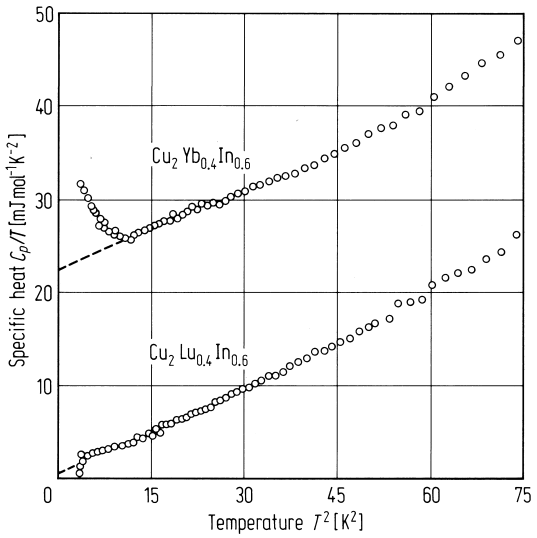

Fig. 359. Specific heat divided by temperature as a function of temperature squared for $Cu_2Yb_{0.4}In_{0.6}$ and $Cu_2Lu_{0.4}In_{0.6}$ at low temperatures [87F1].

X_2YZ X = 4d, Y = 4f

X = 1B: Ag
Y = 4A: La, Ce
Z = 3B: In

The compound Ag_2CeIn orders antiferromagnetically at 2.7 K [87L1]. The specific heat of the La compound was used to estimate the lattice and electronic contributions in Ag_2CeIn.

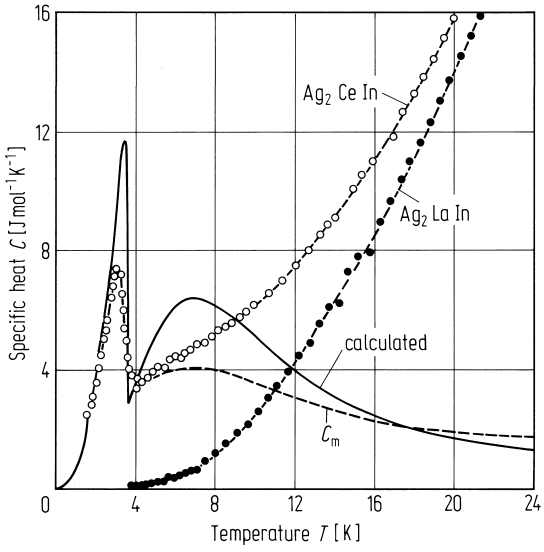

Fig. 360. Specific heat for Ag_2CeIn and Ag_2LaIn. The dashed line is the magnetic contribution C_m above 4 K. The continuous line represents a model calculation using a CEF and exchange Hamiltonian [87L1].

X_2YZ X = 3d, Y = 5f

X = 8A: Ni
Y = 4A: U
Z = 4B: Sn

Owing to the relative size of the actinide atoms, very few compounds form with 5f elements. At room temperature Ni_2USn has the $L2_1$ structure, but transforms at 220 K to a lower symmetry phase.

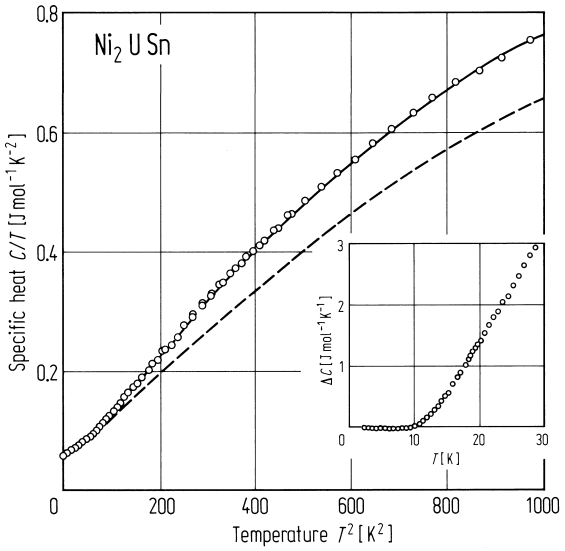

Fig. 361. Specific heat divided by temperature vs. temperature squared for Ni_2USn. The curve is the best overall fit, using electronic plus full Debye contributions. The broken curve is a better two-contribution fit to the low T (< 10 K) data. The inset shows the difference between this fit and the data [90E1].

1.5.5.8 Hyperfine fields

Since the previous review [88W1] a substantial amount of research has been undertaken to determine the hyperfine fields at all three sites. Measurements have also been undertaken as a function of pressure and on systems undergoing phase transitions. Detailed band structure calculations and predictions of hyperfine fields have also been published.

X_2YZ X = 3d, Y = 3d, 4d, 5d,

X = 8A: Co
Y = 4A: Ti, Zr, Hf; 5A: V, Nb; 6A: Cr; 8A: Fe
Z = 3B: Al, Ga; 4B: Si, Ge, Sn

Co_2YZ

The hyperfine field at the Z site has been investigated using ^{119}Sn Mõssbauer effect. Time differential perturbed angular correlating (TDPAC) measurements of Cd hyperfine fields have also been carried out. All the samples are ferromagnetic with the moment confined to the Co sites.

The ^{59}Co and ^{55}Mn NMR have been measured at 4.2 K by the spin echo technique. The measurements at the Y site were carried out by dilute substitution of Mn. The hyperfine field at the Y site was found to be 30-80 kOe higher than that in Co_2 Mn Z alloys with the same Z [89K1].